Geochemistry, Geophysics, Geosystems

RESEARCH ARTICLE
10.1029/2019GC008458

Strain Rate-Dependent Hardening-Softening Characteristics of Gas Hydrate-Bearing Sediments

C. Deusner[1], S. Gupta[1], X.-G. Xie[2], Y. F. Leung[2], S. Uchida[3], E. Kossel[1], and M. Haeckel[1]

[1]GEOMAR Helmholtz Centre for Ocean Research Kiel, Kiel, Germany, [2]Department of Civil and Environmental Engineering, The Hong Kong Polytechnic University, Kowloon, Hong Kong, [3]Civil and Environmental Engineering, Rensselaer Polytechnic Institute, Troy, NY, USA

Key Points:
- The mechanical properties and hardening-softening characteristics of gas hydrate-bearing sediments are dependent on strain rates
- Hardening-softening behavior and strength evolution depend on structural alterations and dynamic rearrangement of gas hydrate-sediment fabrics
- The effects of strain rate-dependent structural alterations can be conceptualized as a nonconstant residual friction term in soil mechanical modeling

Supporting Information:
- Supporting Information S1
- Table S1
- Table S2
- Table S3

Correspondence to:
C. Deusner,
cdeusner@geomar.de

Citation:
Deusner, C., Gupta, S., Xie, X.-G., Leung, Y. F., Uchida, S., Kossel, E., & Haeckel, M. (2019). Strain rate-dependent hardening-softening characteristics of gas hydrate-bearing sediments. *Geochemistry, Geophysics, Geosystems*, *20*, 4885–4905. https://doi.org/10.1029/2019GC008458

Received 22 MAY 2019
Accepted 22 OCT 2019
Published online 8 NOV 2019

Abstract The presence of gas hydrates (GHs) increases the stiffness and strength of marine sediments. In elasto-plastic constitutive models, it is common to consider GH saturation (S_h) as key internal variable for defining the contribution of GHs to composite soil mechanical behavior. However, the stress-strain behavior of GH-bearing sediments (GHBS) also depends on the microscale distribution of GH and on GH-sediment fabrics. A thorough analysis of GHBS is difficult, because there is no unique relation between S_h and GH morphology. To improve the understanding of stress-strain behavior of GHBS in terms of established soil models, this study summarizes results from triaxial compression tests with different S_h, pore fluids, effective confining stresses, and strain histories. Our data indicate that the mechanical behavior of GHBS strongly depends on S_h and GH morphology, and also on the strain-induced alteration of GH-sediment fabrics. Hardening-softening characteristics of GHBS are strain rate-dependent, which suggests that GH-sediment fabrics dynamically rearrange during plastic yielding events. We hypothesize that rearrangement of GH-sediment fabrics, through viscous deformation or transient dissociation and reformation of GHs, results in kinematic hardening, suppressed softening, and secondary strength recovery, which could potentially mitigate or counteract large-strain failure events. For constitutive modeling approaches, we suggest that strain rate-dependent micromechanical effects from alterations of the GH-sediment fabrics can be lumped into a nonconstant residual friction parameter. We propose simple empirical evolution functions for the mechanical properties and calibrate the model parameters against the experimental data.

Plain Language Summary Gas hydrates (GHs) are crystalline-like solids, which are formed from natural gas molecules and water at high pressure and low temperature. GHs, and particularly methane hydrates, are naturally abundant in marine sediments. It is known that the presence of GH increases the mechanical stiffness and strength of sediments, and there is strong effort in analyzing and quantifying these effects in order to understand potential risks of sediment destabilization or slope failure. Based on our experimental results from high-pressure geotechnical studies, we show that not only the initial amount and distribution of GH are important for the increased strength of GH-bearing sediments but also the dynamic rearrangement of GH-sediment fabrics during deformation characterizes the stress-strain response and enables strength recovery after failure. We propose that different microstructural mechanisms contribute to this rearrangement and strength recovery of GH sediment. However, we consider these complicated processes in a simplified manner in an improved numerical model, which can be applied for geotechnical risk assessment on larger scales.

1. Introduction

In marine and permafrost soils, gas hydrates (GH) can be present in large amounts and at high relative saturations (Wallmann et al., 2012). GH formation can occur whenever pressure-temperature (p/T) conditions are inside the GH stability region, and GH-forming components such as CH_4 are available in sufficient amounts. The presence of GH changes the mechanical properties of these sediments or soils, with increased GH saturations (S_h) often being related to higher shear strength, increased stiffness, and stronger dilatancy (e.g., Waite et al., 2009; Yun et al., 2007). The mechanical and hydraulic properties of GH-bearing sediments (GHBS) are considered to influence the stability of marine sediments and slopes (Bugge et al., 1988; Elger et al., 2018; Kvalstad et al., 2005; Mountjoy et al., 2014), and they are crucial factors for drilling operations

(McConnell et al., 2012) and natural gas production scenarios (Boswell et al., 2017; Collett, 2002; Konno et al., 2017; Schoderbek et al., 2012; Yamamoto et al., 2014). Thus, considerable effort is invested in geotechnical testing of GHBS to better understand geomechanical properties and stress-strain behavior in slope failure events or GH production scenarios.

The mechanical effects of different GH formation methods and GH-sediment morphologies and structures have been investigated (Clayton et al., 2005; Dai et al., 2012; Hyodo, Yoneda, et al., 2013; Miyazaki, Masui, et al., 2011; Ning et al., 2012; Winters et al., 2007). GHs in sediments are usually characterized either to be pore-filling and having only a minor effect on stress-strain behavior or to be grain-coating or load-bearing with larger mechanical effects (Hyodo, Li, et al., 2013; Priest et al., 2009). Which type is formed preferentially depends on S_h and the pore fluid composition with a tendency of pore-filling GHs to occur under gas-limited conditions, and grain-coating GHs being formed in water-limited sediments (Choi et al., 2014; Ebinuma et al., 2005; Priest et al., 2009). Experimental studies have evaluated effects of varying S_h (e.g., Masui et al., 2005; Santamarina & Ruppel, 2010), temperatures (Jia et al., 2017; Song et al., 2016), pore pressures (u, Jiang, Zhu, et al., 2015), and effective stresses (σ_3', Lee, Francisca, et al., 2010; Miyazaki, Tenma, et al., 2011) to identify relevant parameters and initial conditions in the geotechnical analysis of GHBS. In particular with the perspective on sand production issues during natural gas production and potential slope failure of fine-grained sediments, the effects of fines content (Hyodo et al., 2017; Jung et al., 2012; Kajiyama, Hyodo, et al., 2017; Lee, Santamarina, et al., 2010; Yun et al., 2007), lithology and consolidation history (Fujii et al., 2015; Ito et al., 2015; Santamarina et al., 2015; Suzuki et al., 2015; Yoneda et al., 2015a), and thermo-hydro-chemo-mechanical process coupling (Gupta et al., 2017; Klar et al., 2013; Sánchez et al., 2017; Uchida et al., 2016) have received attention.

The presence of GH is often considered to have a cohesive or cementing effect, which contributes to sediment strength in addition to friction and dilatancy. The nature and mechanism of a potential cohesion or cementation effect of GH is still unclear (Jung & Santamarina, 2011; Pinkert, 2017; Priest et al., 2009). Recently, experimental studies on microscale GH-sediment fabrics have indicated the presence of a water layer between GH and quartz sand particles (Chaouachi et al., 2015), which appears to contradict the assumption of cementation or true cohesion. However, the study of microscale GH-sediment fabrics is a very active field of research (Lei et al., 2018; Lei et al., 2019). For simplicity, in this study we refer to a structuration effect for evaluation of experimental data and for constitutive modeling, without referring to a particular micromechanical effect.

Time- and rate-dependent effects on the stress-strain behavior of GHBS have received less attention in the past. However, viscous deformation and creep strain of GHBS were reported to be relevant (Miyazaki et al., 2010) and similar to frozen sand (Miyazaki et al., 2017). Experiments on pure GH have shown high stiffness, strength, and ductility, as well as the relevance of strain-induced structural alterations (Durham et al., 2003; Jia et al., 2016; Stern et al., 1996).

Several studies have analyzed the mechanical behavior of GHBS during and after GH dissociation through depressurization or thermal stimulation (Hyodo, Yoneda, et al., 2013; Hyodo et al., 2014; Song et al., 2014). In the very recent past there have also been the first attempts to carry out studies on undisturbed pressure cores (Inada & Yamamoto, 2015; Santamarina et al., 2015; Yoneda et al., 2015b). Advanced geotechnical testing systems with tomographical techniques are increasingly being developed and used to analyze so far unresolved microstructures and micromechanical processes that constitute bulk stress-strain behavior in GHBS (Deusner et al., 2016; Yoneda et al., 2016).

Numerical GH reservoir simulators have been used to study the behavior of GHBS during gas production (Gupta et al., 2015; Rutqvist et al., 2009; Rutqvist et al., 2012) or in marine slope destabilization (Jiang, Sun, et al., 2015; Sultan & Garziglia, 2014; Zander et al., 2018), and there is strong effort to improve soil mechanical constitutive models and model couplings. A number of nonlinear elastic (Miyazaki, Aoki, et al., 2011; Yu et al., 2011) and elasto-plastic (Klar et al., 2010; Lin et al., 2015; Sun et al., 2015; Uchida et al., 2012) constitutive models have been proposed. Furthermore, elasto-viscoplastic models have been considered (Kimoto et al., 2010). Discrete element methods (DEM) have been applied to analyze micromechanical interactions and the role of phase distributions in GHBS (Brugada et al., 2010; Shen et al., 2016; Shen & Jiang, 2016).

Here we analyze the hardening-softening behavior of GHBS using a combined experimental-numerical approach. We investigate the stress-strain behavior of gas- and water-saturated GHBS at different S_h, GH-sediment fabrics, effective stresses, and strain rates in triaxial compression tests. The experimental

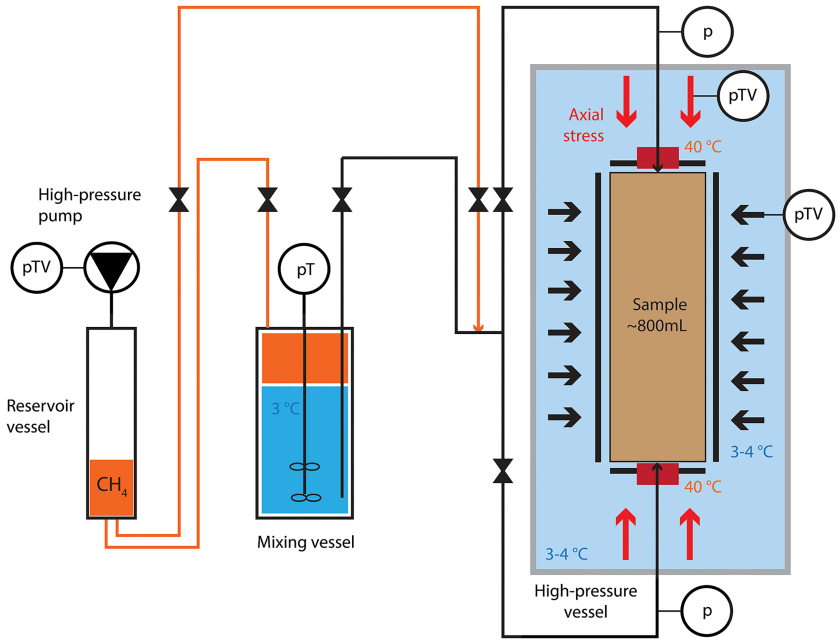

Figure 1. Experimental scheme.

data are used to develop a constitutive model and to carry out preliminary parameter calibration and model testing.

2. Materials and Methods

2.1. Experimental Setup

Experiments were carried out in the high-pressure flow-through system NESSI (*Natural Environment Simulator for Subseafloor Interactions*) that was equipped with a triaxial cell mounted in a 40-L stainless steel vessel (Figure 1, Deusner et al., 2012; Deusner et al., 2017; Gupta et al., 2017). All wetted parts of the setup are made of stainless steel. Temperature control was achieved through the hydraulic fluid (glycol-water mixture) inside the pressure vessel using a heat exchanger and a thermostat system (T1200, Lauda, Lauda-Konigshofen, Germany). Confining and axial stresses acting on the sample were controlled by two high-precision hydraulic pumps and actuators (VPC 400, APS GmbH, Rosdorf, Germany). The change of sample volume was calculated by the changes of hydraulic fluid volumes for axial and confining stress-strain control. The pore pressure was regulated by a high-precision piston pump (Teledyne ISCO, Lincoln NE, USA), which was connected to top and bottom platens of the triaxial cell through high-pressure fluid reservoirs with water or gas, respectively (Parr Instruments, Illinois, USA). The pore pressure was monitored in the influent and effluent tubings of the triaxial cell. Initial pressurization with CH_4 and water exchange after GH formation was carried out using fine-regulating valves (TESCOM Europe, Selmsdorf, Germany).

2.2. Sample Preparation and Mounting

Sediment samples were prepared from quartz sand (porosity 0.35, grain size 0.1–0.6 mm, mean particle diameter 0.29 mm, G20TEAS, Schlingmeier, Schwülper, Germany; see supporting information S3), and mixed with defined amounts of deionized water. The partially water-saturated and homogenized sediments were filled into the triaxial sample cell, which was equipped with a combination of a fluoroelastomer (FKM) sleeve and a latex rubber sleeve to obtain final sample dimensions of 160 mm in height and 80 mm in diameter (supporting information Figure S2). The sand was placed in five layers, with each layer being tamped 30 times. Sample geometry was assured using a sample-forming device. The sample was cooled to 3–4 °C after the triaxial cell was mounted inside the pressure vessel. Temperature inside the pressure vessel was monitored throughout the experiments.

2.3. GH Formation and Pore Fluid Exchange

GH formation was carried out in normally consolidated samples at constant isotropic effective stress of 1 MPa using an excess gas method (Hyodo, Li, et al., 2013; Masui et al., 2005; Waite et al., 2004). To avoid effective stress changes, flow-controlled slow pressurization with CH_4 was achieved using fine-regulating valves, while the confining stress was regulated accordingly. After pressurization, influent and effluent pore pressure valves were closed. Pore pressure was not regulated during GH formation, whereas isotropic effective stress was automatically controlled at 1 MPa. The target GH saturation (S_h) was defined by the amount of deionized water in the sample with an estimated error of ±1.25% due to the sequence of steps for sample preparation and mounting. In addition, initial S_h in the compression tests was calculated based on pore pressure measurements and sample temperature monitoring during GH formation, assuming a hydration number of 5.75. Taking into account various sources of uncertainty in this calculation (see supporting information S4 for further discussion), GH formation was estimated as being completed by 85 ± 19% prior to testing (supporting information Table S1) relative to the target S_h value. Here we referred to this estimate and took into account that small amounts of water might have been available at the onset of the compression tests. Mechanical tests were started earliest after a hold time of 3 days and latest after 15 days, referring to the end of pressurization with CH_4.

Prior to testing, some samples were saturated with water whereby remaining CH_4 gas was replaced with deionized water, which was either saturated with CH_4 or free of dissolved CH_4, respectively. Saturation with CH_4 was achieved in a stirred pressure vessel within 24 h at slightly higher pressures and lower temperatures compared to p/T conditions in the triaxial cell. Gas-water replacement was carried out after reducing the pore pressure to approximately 0.5 MPa above GH stability conditions, by percolating water in upstream mode at a flow rate of 100 mL/min at constant isotropic effective stresses. CH_4 gas and percolated water were collected in a pressurized reservoir.

2.4. Triaxial Compression Testing

Strain-controlled drained triaxial compression tests were performed after individual hold periods (supporting information Table S1). The tests were carried out at axial strain rates 0.006, 0.06 and 0.6%/min, and at constant minor principal stresses of 0.25, 0.5, and 1.0 MPa. Pressure, stress, and strain measurements were recorded every 1 s. Data were averaged over time intervals of 1 min prior to evaluation. The accuracy of the individual pressure measurements is ±0.5% at constant temperature. Random errors resulting from temperature changes or leakage of fluids can be neglected due to the short duration of the compression tests and large thermal buffer capacity of the high-pressure systems. The accuracy of volume and strain measurements is related to pressure measurements since system volume changes are calibrated depending on the system pressure. Thus, erroneous pressure measurements can result in an overall error of volume measurement of 4 mL, which converts to 0.4% of volumetric strain. The effective confining stress (σ_3') was controlled with an accuracy of ±0.5% throughout the individual compression tests. However, in few occasions minor and short deviations from the specified values were observed due to rapid volume change events or experimental problems. We highlight issues with confining stress control in the figure captions and provide the measurement results for all compression tests (supporting information S5).

2.5. Constitutive Modeling and Numerical Simulation

We consider a classical plasticity framework (Jirasek & Bazant, 2002), where the state of stress depends on the loading-unloading history and is calculated incrementally. The total infinitesimal strain $\underset{\sim}{\varepsilon} := \frac{1}{2}\left(\nabla \boldsymbol{u} + \nabla^T \boldsymbol{u}\right)$, where $\boldsymbol{u}$ denotes the displacement field, is decomposed additively into the elastic strain $\underset{\sim}{\varepsilon}^e$ and the plastic strain $\underset{\sim}{\varepsilon}^p$, that is, $\underset{\sim}{\varepsilon} = \underset{\sim}{\varepsilon}^e + \underset{\sim}{\varepsilon}^p$. In the elastic range, we assume linear isotropic material behavior with Young's modulus E and Poisson's ratio ν as the model parameters.

2.5.1. Yield Function and Plastic Flow Rule

There exists a yield surface F in the stress space that encompasses the elastic region. The stress states lying inside the yield surface produce elastic deformations, while the stress states lying on the surface produce plastic deformations. The stress states outside the yield surface are inadmissible. We consider a Drucker-Prager yield criterion where the yield function is given as

$$F\left(\underset{\sim}{\sigma},\chi\right) := q + \alpha(\chi)p - c = 0 \tag{1}$$

Here $p := \frac{1}{3} Tr\underset{\sim}{\sigma}$ and $q := \sqrt{\frac{3}{2}} \left\| \text{dev } \underset{\sim}{\sigma} \right\|$ are the stress invariants. p denotes hydrostatic or mean stress, and q denotes shear stress. Function F describes a conical surface in the principal stress space, s.t. the axis of the cone coincides with the hydrostatic line. Parameter α indicates the mobilized frictional resistance at any given stress state, and c indicates a structuration parameter. χ denotes the vector of internal plastic variables that affect the hardening-softening behavior of GHBS. Similar to the yield surface F, there exists a plastic potential surface G in the stress space such that the plastic flow occurs in a direction normal to this surface. The incremental plastic strains can be derived from the plastic potential G as

$$\underset{\sim}{\dot{\epsilon}}^p = \dot{\lambda} \frac{\partial G}{\partial \underset{\sim}{\sigma}} \tag{2}$$

where $\partial G / \partial \underset{\sim}{\sigma}$ describes the normal to the surface G, and $\dot{\lambda}$ is a proportionality constant indicative of the magnitude of the plastic strain increment. Furthermore, it can be shown that the invariants of the plastic strain rate can be written as

$$\dot{\epsilon}_v^p := Tr\underset{\sim}{\dot{\epsilon}}^p = \dot{\lambda} \frac{\partial G}{\partial p} \quad \text{and} \quad \dot{\epsilon}_s^p = \sqrt{\frac{2}{3}} \left\| \text{dev } \underset{\sim}{\dot{\epsilon}}^p \right\| = \dot{\lambda} \frac{\partial G}{\partial q} \tag{3}$$

We consider a non-associative flow rule, that is, $G \neq F$

$$G\left(\underset{\sim}{\sigma},\chi\right) := q + \beta(\chi)p = 0 \tag{4}$$

with $\beta < \alpha$. The parameter β denotes the dilatancy of the material.

2.5.2. Consistency Conditions

Along any process of loading-unloading, if $F < 0$, the stress state is elastic and $\dot{\lambda} = 0$, while, if $F = 0$, the stress state is plastic and $\dot{\lambda} > 0$. These nonlinear inequality constraints can be reformulated as the following Karush-Kuhn-Tucker (Kuhn & Tucker, 1951) optimality conditions:

$$F\left(\underset{\sim}{\sigma},\chi\right) \leq 0, \quad \dot{\lambda} \geq 0, \quad \dot{\lambda} F = 0. \tag{5}$$

To confine the stress trajectory to the yield surface during plastic loading, an additional plastic consistency condition is considered (de Souza Neto et al., 2008):

$$\dot{\lambda}\dot{F} = \dot{\lambda}\left(\frac{\partial F}{\partial \underset{\sim}{\sigma}} : \underset{\sim}{\dot{\sigma}} + \frac{\partial F}{\partial \chi} : \dot{\chi}\right) = 0 \tag{6}$$

2.5.3. Numerical Solution and Calibration Procedure

We solve the global nonlinear equilibrium equation using a Galerkin finite element formulation defined on Q1 elements. The nonlinearities are resolved iteratively using a full Newton-Raphson method with a continuum tangent matrix (Zienkiewicz & Taylor, 2014). Within each global Newton iteration step, a local problem is solved at each Gauss point to determine the new stress state. The local problem involves the integration of the material constitutive model over the load increment of the current global step. We use an implicit return mapping algorithm (Huang & Griffiths, 2009; Simo & Hughes, 2006) to solve the local problem. We have implemented our numerical scheme in C++ based on the DUNE PDELab framework (Bastian et al., 2010; Dedner et al., 2010).

For numerical simulation of the triaxial compression experiments and model calibration, we consider a one element triaxial setup with unit dimensions (supporting information Figure S1). Load is applied in two stages. In the first stage, an isotropic load equal to the confining stress is applied, which

corresponds to the initial stress state of the GHBS sample. In the second stage, strain-controlled triaxial compression is simulated by specifying an axial strain rate corresponding to vertical displacement rates in the experiments. We use a regression based parameter estimation strategy and test the goodness-of-fit against the experimental data using a weighted R^2 measure where higher weights are assigned to the data points in the elastic region, in the vicinity of the peak strength, and along the secondary hardening curve. In this study, we used a heuristic strategy because our objective was to identify the *trends* in the parameter space and not to find the *best fit* for the parameters. For future parameter estimation studies, we are developing Bayesian inversion frameworks based on an Active Subspaces method for model reduction (Teixeira Parente et al., 2018).

3. Results

3.1. Experimental Results

The stress-strain behavior of GH-free sand was taken as reference in this study. The behavior of this reference sample specimen was similar for water-saturated, partially dry and dry sand (Figure 2) and typical for medium dense sand. The critical state friction angle (φ_{cs}) was calculated to be 33.3 ± 1° based on peak friction angles φ_{max} and maximum dilation angles ψ_{max} (supporting information Table S3) according to equation (7) (Bolton, 1986; Schanz & Vermeer, 1996):

$$\varphi_{cs} = \varphi_{max} - 0.5\psi_{max} \tag{7}$$

Dilation angles were calculated based on changes in volumetric ($\partial\varepsilon_{p'}$) and deviatoric strains ($\partial\varepsilon_q$):

$$\sin\psi = -\frac{\frac{\partial\varepsilon_{p'}}{\partial\varepsilon_q}}{2-\frac{\partial\varepsilon_{p'}}{\partial\varepsilon_q}} \tag{8}$$

Critical state conditions that are defined to occur without volumetric strain were not reached in the range of axial strains investigated in this study, which is, however, typical (e.g., Omidvar et al., 2012). Apparent oscillations of dilatancy index d (equation (9)) result from time-resolved calculations based on small strain increments.

$$d = \frac{\partial\varepsilon_{p'}}{\partial\varepsilon_q} \tag{9}$$

The analysis of the results within the scope of Rowe's stress-dilatancy theory (Rowe, 1962) and using equation (10) (Porcino & Marcianò, 2017; Yu et al., 2007) to calculate reference lines for different values of c'/p'(c': structuration strength, p′: mean effective stress) clearly indicates contributions of friction and dilation to reference sediment strength. The stress ratio η is defined according to equation (11) (q: deviatoric stress, $M = 1.342$: frictional constant defining the critical slope line). As expected, no cohesion or structuration strength (c') was observed, and data plot on the $c'/p' = 0$ line (Figure 2c). The parameter c', which refers to Mohr-Coulomb shear strength criteria, relates to the structuration parameter c (equation (1)) according to equation (12) (e.g., Wojciechowski, 2018).

$$d = \frac{9(M-\eta) + 6\frac{c'}{p'}\sqrt{3+2M(3-M)}}{9+3M-2M\eta+4\left(\frac{c'}{p'}\right)\sqrt{3+2M3-M}} \tag{10}$$

$$\eta = \frac{q}{p'} \tag{11}$$

$$c = \frac{6c'\cos\varphi}{\sqrt{3}(3-\sin\varphi)} \tag{12}$$

The stress-strain behavior of gas-saturated GH-bearing sand showed strong hardening-softening behavior and substantially increased peak strength compared to GH-free sand (Figures 2d–2g). The stiffness of

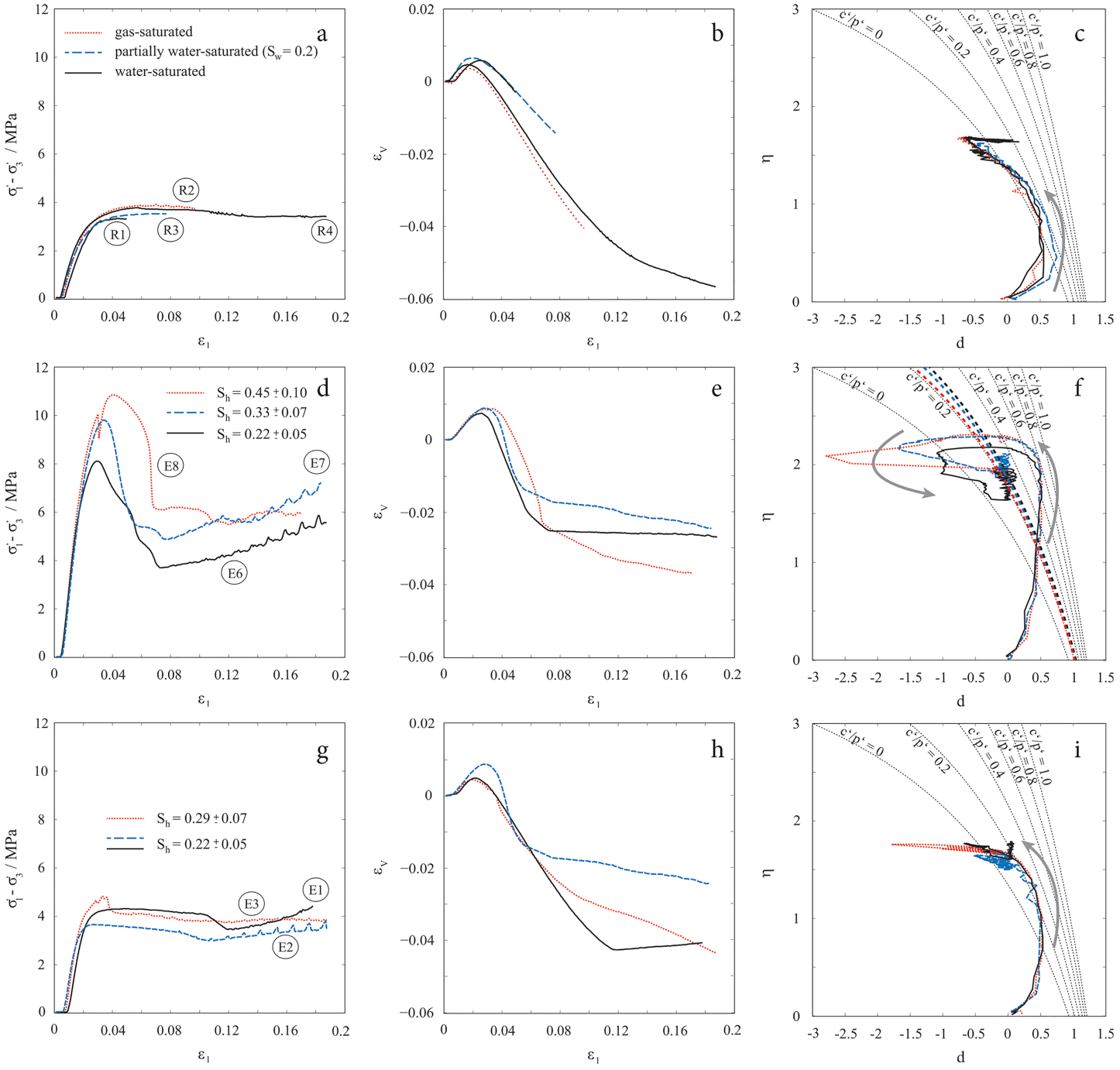

Figure 2. Results from compression tests with GH-free sand (a–c), gas-saturated GH-bearing sand (d–f), and water-saturated GH-bearing sand (g–i). (a, d, g) Strength characteristics, (b, e, h) volumetric strain, and (c, f, i) stress-dilatancy relationship. Labels refer to test numbers in supporting information Tables S1–S3. Remarks: (d) The brief drop in (σ_1-σ_3) at $\varepsilon_1 \approx 0.03$ in the test with $S_h = 0.45$ was due to test interruption for technical reasons. (g) The oscillations in (σ_1-σ_3) at $\varepsilon_1 \approx 0.02$–$0.03$ in the test with $S_h = 0.29$ were due to transient problems with pore pressure regulations and differences between pressure values u_1 and u_2. The maximum error in effective stress conditions (σ_3') was minor ($\approx 3\%$) and, thus, neglected in further data analysis.

GHBS was higher than GH-free samples, but it did not show a clear dependence on S_h in the tested range (supporting information Figure S6). However, the peak strength showed a clear dependence on S_h (Figure 2d). The onset of dilation was similar at different S_h and largely coincided with peak strength. Thus, different from the GH-free sand, the occurrence of peak strength and peak dilation was clearly separated and the substantial increase in peak strength could not be assigned to merely sediment friction

and dilation. The post-peak behavior indicated that after passing peak strength, dilatancy was rapidly mobilized and the cumulative volumetric strain approached values of GH-free sand. Post-peak residual strength of GH-bearing samples approached values of GH-free sand in only few cases and mostly stayed above reference values. However, after partial mobilization of dilatancy during softening, further dilation was effectively suppressed and strain behavior indicated arrival at critical state conditions. The clear transition in strain behavior suggests strain localization and mobilization in a narrow shear zone. Post-peak strength minima showed some relation to S_h in the order of magnitude of differences at peak strength.

Evaluation of the results within the scope of Rowe's theory clearly suggests that the presence of GH contributes a strong structuration effect (colored dashed lines in Figure 2f; supporting information Table S3). Conspicuously, the stress-strain behavior after softening until the end of the tests showed an apparent secondary hardening effect, which resulted in the recovery of peak structuration strength (Figure 2f). This apparent strength recovery was more pronounced in cases where dilatancy was most suppressed, and thus, ongoing deformation occurred in a narrower shear zone.

In water-saturated samples in which the pore space was flushed after completion of GH formation, the stress-strain response was very different compared to gas-saturated samples. The peak strength and hardening-softening behavior were strongly suppressed (Figures 2g–2i). Post-peak dilation was considerably larger and extended over longer time and strain intervals, similar to the observed response in GH-free sand. This suggests that strain was not confined to a narrow shear zone as it was observed in tests without water flushing. Only a minor structuration effect was observed in the early compression phase (Figure 2i), and post-peak strain behavior could be attributed to reference sand residual friction.

Tests on gas-saturated samples at different effective confining stresses (0.25–1 MPa) and S_h (Figure 3) were largely in accordance with Figure 2. Peak strength values were dependent on S_h, and samples showed a clear hardening-softening behavior. The post-peak behavior was characterized by a rapid mobilization of dilatancy and a sharp transition in volumetric strain evolution with reduced dilatancy, which indicates strain localization in a narrow shear zone. The width of the strength peak appeared to be dependent on effective stresses. Low initial effective stresses resulted in more brittle failure and faster strength depletion during softening. At higher effective stresses, the peak was substantially broader, and failure characterized by higher ductility and slower softening. Similar to tests at different S_h (Fig.2, Supplementary Table S2), there was no obvious difference in stiffness properties or primary hardening, except that the magnitude of compression was higher at higher effective stresses. Structuration estimates (c', supporting information Table S3) at the onset of dilation (1.2–2.1 MPa) and peak strength (0.9–1.4 MPa) were similar at different effective stresses and showed a dependency on S_h. Highest stress ratios (η) at peak strength were observed at lower effective stresses (approximately 2.7). The softening intervals were again followed by apparent strength recovery, which proceeded toward peak structuration strength of individual samples (colored dashed lines in Figures 3c, 3f, and 3i). A second softening event in the later strain period ($\varepsilon_1 \approx 0.16$) led to further mobilization of dilatancy and was followed by strength recovery in the late compression stage.

The stress-strain response was strongly dependent on strain rates in the range between 0.006 and 0.6%/min (Figure 4). Faster strain rates resulted in stiffer behavior and earlier arrival at peak strength. The magnitude of compression prior to softening was lower at high strain rates. This behavior was similarly observed at different S_h. Softening was considerably more brittle at fast strain rates, with substantial differences in strength peak width and earlier mobilization of dilatancy. The magnitude of peak strength, however, was only affected to a minor extent. Rapid mobilization of dilatancy after peak strength and strain softening behavior were observed in all tests with a sharp transition in dilation behavior after softening. The amount of mobilized dilatancy, however, was dependent on strain rates, with a smaller amount of dilatancy being mobilized at higher strain rates. This suggests that brittle failure at faster strain rates occurred in a narrower failure zone compared to more ductile deformation at slow strain rates. Again, post-peak behavior in all tests was characterized by apparent recovery of peak structuration strength. At higher S_h and faster strain rates, mobilization of dilatancy appeared to be occurring stepwise with a brief strength plateau after first rapid softening, which suggests the occurrence of additional transient strengthening effects as a consequence of fast and brittle failure.

The transient increase of isotropic effective stress by 1 order of magnitude to 10 MPa prior to triaxial compression tests had only minor effects on the stress-strain behavior compared to strain rate effects (supporting information Figure S8). In addition to increase in stiffness, compressive strain prior to peak strength was

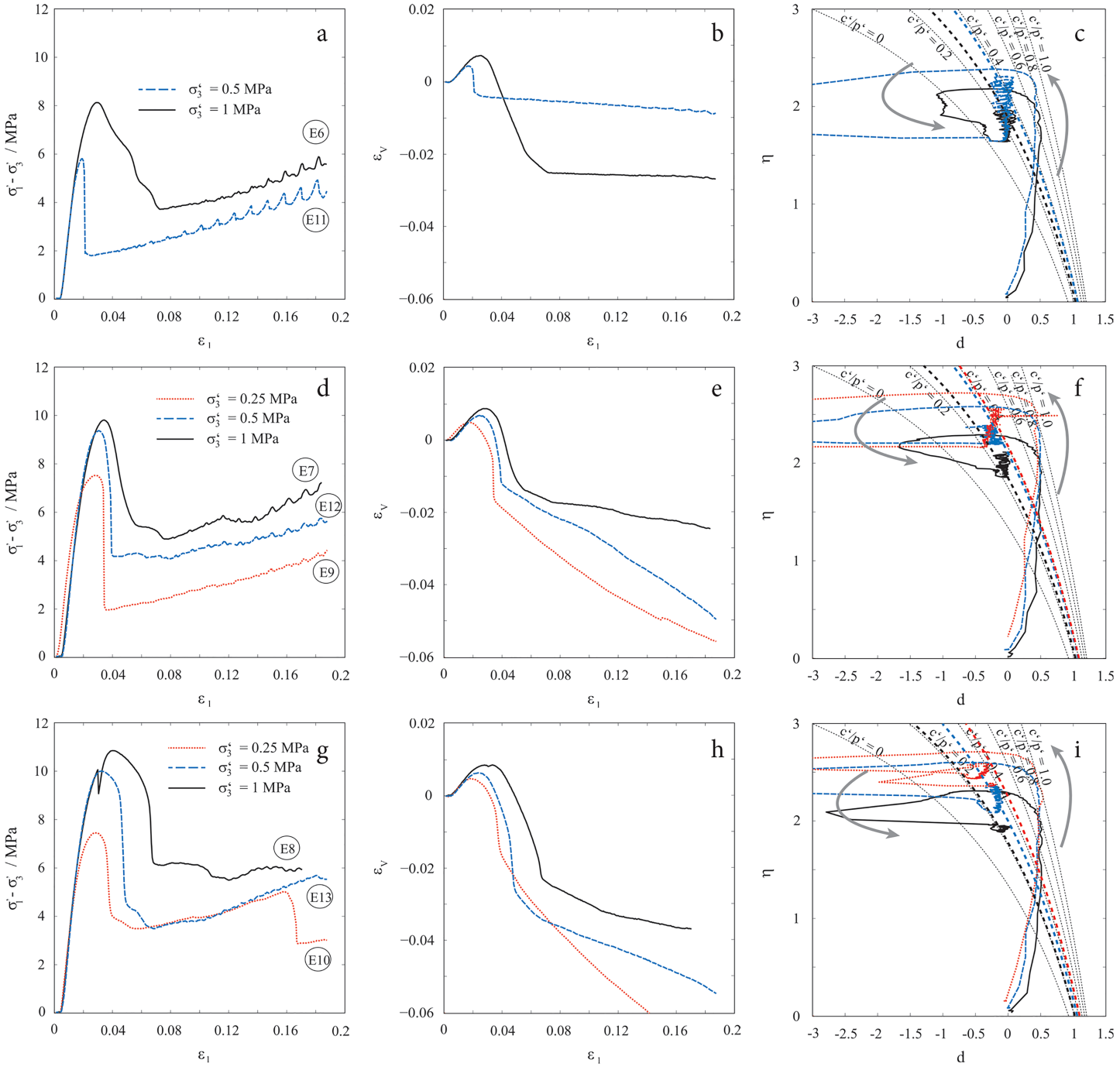

Figure 3. Results from compression tests with gas-saturated GH-bearing sand at different effective confining stress (σ_3'), (a–c) $S_h = 0.22$, (d–f) $S_h = 0.36$, (g–i) $S_h = 0.45$. (a, d, g) Strength characteristics, (b, e, h) volumetric strain, and (c, f, i) stress-dilatancy relationship. Labels refer to test numbers in supporting information Tables S1–S3.

expectedly lower than for normally consolidated samples, and softening revealed a more brittle behavior. However, peak strength was only slightly affected, which suggests that GH-sediment fabrics were not substantially altered in response to transient isotropic loading.

Additional test results suggest that the hold time after completion of GH formation can strongly influence the stress-strain characteristics in compression tests. A test of a water-saturated specimen ($S_h = 0.22$) after a hold time of 15 days after pressurization with CH_4 and transient increase of isotropic effective stress by 1

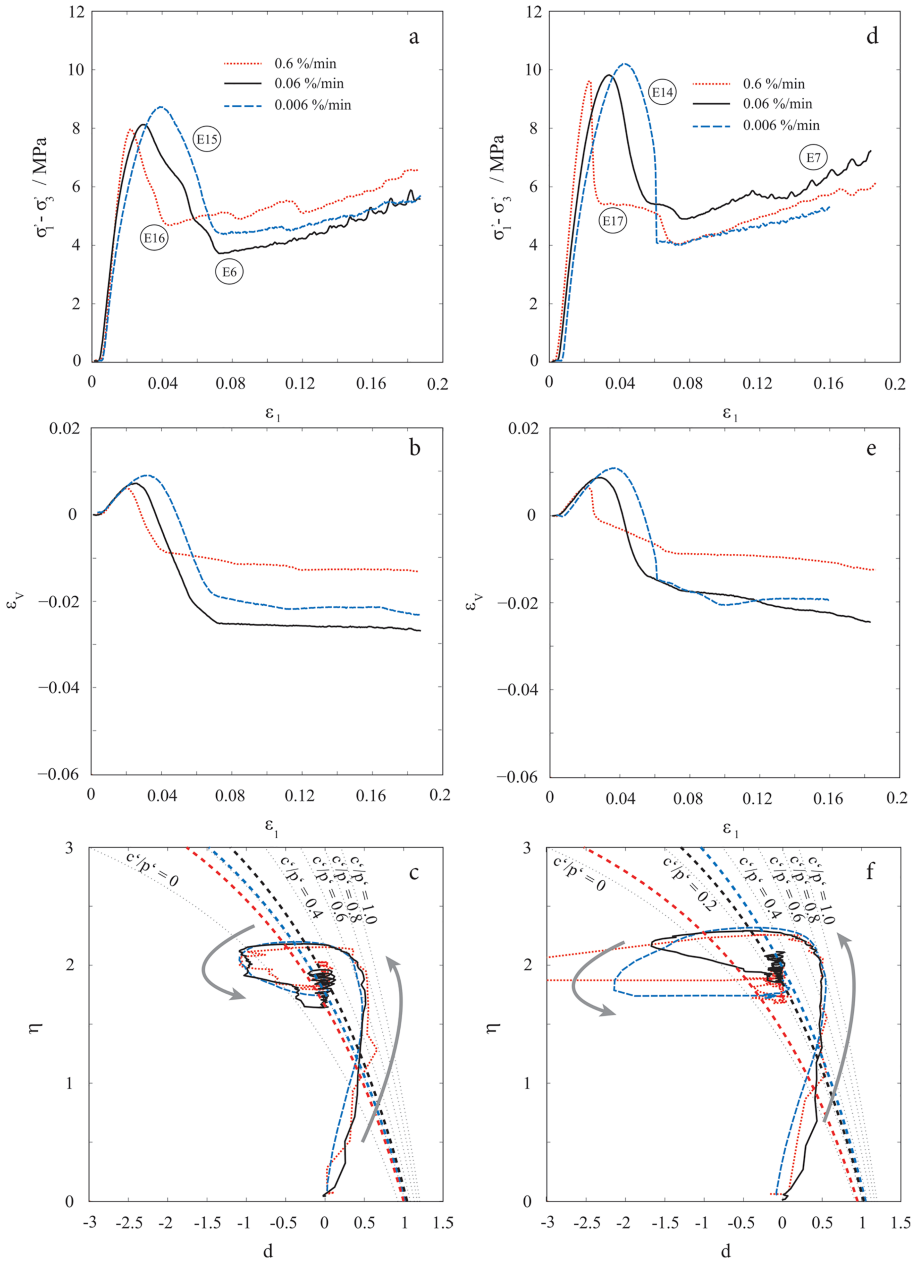

Figure 4. Results from compression tests with gas-saturated GH-bearing sand at different strain rates: (a–c) $S_h = 0.22$, (d–f) $S_h = 0.33$–0.36, (a, d) strength characteristics, (b, e) volumetric strain, and (c, f) stress-dilatancy relationship. Labels refer to test numbers in supporting information Tables S1–S3.

order of magnitude to 10 MPa prior to deviatoric loading showed clear changes in stress-strain behavior (E20, supporting information Table S1 and Figure S9). Although stiffness properties and early yielding behavior appeared to be unaffected, peak strength and softening were not observed. After limited initial compression and similar onset of dilation, dilation characteristics showed a smooth transition toward zero volumetric strain with continuous increase of deviatoric stress.

3.2. Modeling Studies

To consider strain rate effects in constitutive modeling, the model parameterization is based on the assumption that the total mobilized frictional resistance (α) can be decomposed into a residual friction component (α_{res}) and a dilatancy component (β, e.g., Houlsby, 1991).

$$\alpha = \beta + \alpha_{res} \tag{13}$$

Dilatancy is a macroscopic manifestation of the kinematic constraints imposed by the microstructure of the soil skeleton and evolves through any micromechanical process that causes volume changes of the soil. The residual friction, on the other hand, is an intrinsic property of the skeleton and can usually be assumed constant for intact quasi-static soils. In the transition from solid-like to fluid-like behavior, however, the residual friction of a dynamic soil skeleton is expected to change at different strain rates (Andrade, et al., 2012). Here this concept was modified and extended to model strain and strain rate effects for GHBS during different hardening-softening intervals.

In order to develop the evolution functions for the model parameters, we consider the internal variables $\chi = (\chi_1, \chi_2)^T$, where $\chi_1 = (S_h, \dot{\epsilon}_1)$ denotes the *explicit* internal variables that arise from the test conditions but remain constant during plastic deformation, while $\chi_2 = (\dot{\lambda}, \lambda)$ denotes the *implicit* internal variables that arise from plastic deformation (refer to equation (2)). Based on the experimental observations, we introduced smooth evolution functions for the parameters β and α_{res}

$$\beta = \beta_{max}(\chi_1) \cdot \bar{\lambda} \cdot \exp\left(1 - \bar{\lambda}^{\frac{3}{4}}\right) \tag{14}$$

$$\alpha_{res} = \alpha_{min}(\chi_1) + \Delta\alpha_{res}(\chi_1) \cdot \left(1 + 1/\dot{\bar{\lambda}}\right)^{-1} \cdot \bar{\lambda} \tag{15}$$

where $\bar{\lambda} = \lambda/\lambda^*(\chi_1)$ and $\dot{\bar{\lambda}} = \dot{\lambda}/\dot{\lambda}^*(\chi_1)$.

Equations (14) and (15) are extensions of the evolution functions proposed in Andrade, et al. (2012). β_{max} denotes the peak dilatancy, and λ^* denotes the corresponding accumulated plastic shear strain. α_{min} denotes the initial frictional resistance of the intact material before loading, and $\dot{\lambda}^*$ denotes the critical plastic strain rate. To understand the significance of $\dot{\lambda}^*$, note that in equation (15), $\left(1 + 1/\dot{\bar{\lambda}}\right)^{-1} \leq 1$, and $\dot{\lambda}^*$ controls the growth rate of this function. The smaller the value of $\dot{\lambda}^*$, the faster the function grows to its maximum value. Note that for each triaxial test, since χ_1 remains constant throughout the test, the model parameters β_{max}, α_{min}, and $\Delta\alpha_{res}$ also remain constant but have different values for each test. In this work, we do not propose any functional relationship for the evolution of these parameters wrt χ_1 but rather infer the parameter values from the experimental data and study whether consistent trends emerge.

Our elasto-plastic model has an eight-dimensional parameter space, $\mathcal{P}(\chi_1) = \left(E, \nu, c, \alpha_{min}, \Delta\alpha_{res}, \beta_{max}, \lambda^*, \dot{\lambda}^*\right)^T$. E, ν parameterize the elastic model, c, α_{min} the initial yield surface, and $\Delta\alpha_{res}, \beta_{max}, \lambda^*, \dot{\lambda}^*$ control the subsequent hardening-softening of the yield surface. The combination of E, ν, c, α_{min} characterizes the *initial state* of the test sample, before loading begins. The parameters in $\mathcal{P}$ were calibrated against the experimental data following the procedure outlined in section 2.5.3. The calibrated parameters for each triaxial test are listed in Table 1, where the first two columns represent χ_1, the rows E2 and E3 denote the water-saturated samples, and the rows from E6 to E17 refer to the gas-saturated samples.

The parameter estimation confirmed that in our experiments E and ν did not depend noticeably on χ_1 and also appeared to show no clear dependence on the pore fluid. The structuration parameter c showed dependence on the pore fluid but not on χ_1, and α_{min} showed no dependence on both χ_1 as well as pore fluid composition. This suggests that the initial state of the GHBS samples in each test was similar despite having different S_h; however, it differed from that of the reference sand. So, it appears that in our experiments the formation of GH alters the sediment fabric, but the actual quantity of GH (up to the saturations that were investigated) does not affect the nature of this alteration. The peak dilatancy of the GHBS samples showed some correlation with S_h but appears to be independent of the axial strain rate. The progress of dilatancy mobilization, however, is controlled by the strain rate (see parameter $\bar{\lambda}$: the lower $\bar{\lambda}$, the higher will be the rate of dilatancy mobilization in accordance with equation (14)). For a given S_h, the higher the strain rate, the faster the dilatancy is mobilized and critical state conditions are established. Further, in the gas-saturated samples, the peak dilatancy and the dilatancy mobilization rate were observed to be higher compared to the water-saturated samples.

The preliminary model calibration focused on matching the strength evolution during primary and secondary hardening within a classical elasto-plasticity framework. It can be seen that this approach, together with

Table 1
Calibrated Model Parameters

	S_h (%)	$\dot{\epsilon}_1$ (min^{-1})	E (MPa)	υ (−)	c (MPa)	α_{min} (−)	$\Delta\alpha_{res}$ (−)	β_{max} (−)	$\dot{\lambda}^*$ (−)	λ^* (−)
E2	22 ± 5	0.0625	475	0.32	0.15	0.72	0.175	0.29	0.0000575	0.025
E3	29 ± 7	0.0625	475	0.32	0.15	0.72	0.2	0.34	0.0000575	0.025
E6	22 ± 5	0.0625	475	0.32	1	0.72	0.175	0.52	0.000285	0.0075
E7	33 ± 7	0.0625	475	0.32	1	0.72	0.375	0.605	0.000285	0.0085
E8	45 ± 10	0.0625	475	0.32	1	0.72	0.5	0.65	0.000285	0.012
E14	36 ± 8	0.00625	475	0.32	1	0.72	0.05	0.605	0.000001	0.0155
E15	22 ± 5	0.00625	475	0.32	1	0.72	0.035	0.52	0.000001	0.0155
E16	22 ± 5	0. 625	475	0.32	1	0.72	0.3	0.52	0.0065	0.00375
E17	36 ± 8	0. 625	475	0.32	1	0.72	0.325	0.605	0.0065	0.0054

Note. Labels refer to test numbers in supporting information Tables S1–S3.

the evolution functions 14 and 15, is able to capture the observed hardening-softening behavior as a function of plastic strains and strain rates (Figure 5). As mentioned in section 2.5.3, the model calibration algorithm attached higher weights to the peak strength and secondary hardening curves. This has led to deviations between experimental and simulation data for unloading during the softening periods. To some extent, the model also underpredicts sample contraction during primary hardening, which follows from the inherent limitations of the Drucker-Prager theory of plasticity. It needs to be noted that large-strain compression test data can be biased by experimental artifacts, for example, platen effects, which would interfere with model calibration.

4. Discussion

4.1. Characteristics of Stress-Strain Behavior of GHBS

This study confirms that the presence of GH alters the stress-strain behavior of sandy sediments. After GH formation from partially water-saturated sand using an excess-gas-method, the GHBS is substantially stiffer and stronger than the GH-free sand (supporting information Tables S2 and S3). The peak and critical strength of water-limited samples, in which the residual gas was not replaced after GH formation, were substantially higher than in water-saturated specimen, in which the residual gas was replaced with water prior to testing. Since the experimental results did not show a large difference after gas replacement with CH_4-free or CH_4-saturated water, that is, at different thermodynamic constraints with respect to GH stability (supporting information Figure S7), the change in mechanical properties is unlikely to be caused by GH dissociation or dissolution. Also, it is unlikely that mechanical damage from hydrodynamic shear forces during pore fluid exchange was responsible for sediment weakening, since water replacement was carried out at relatively low flow rates (100 mL/min). Instead, since the early stress-strain behavior of GH-bearing samples after water exchange still resembled the behavior of gas-saturated samples (supporting information Table S2 and Figure S6), it is likely that the alteration of GH-sediment fabrics and stress-strain behavior were controlled by sample deformation in the presence of water, and not by the exchange of fluid itself.

The stress-strain behavior of GHBS does not show a simple dependency from S_h. A clear dependency with S_h was observed for the magnitude of peak strength, which increases for higher S_h under varying strain and strain rate conditions, given that the pore fluid composition during testing was similar (Figure 6a). At similar strain rates, other parameters show a dependency on S_h, including magnitudes of post-peak strength, strength peak width, ductility characteristics, and axial strain differences between onset of dilation and peak strength. Early yielding and post-peak stress-strain behavior appear to be less related to S_h (supporting information Table S3).

The compression test data from gas-saturated GHBS were characterized by high peak strength values and pronounced strength depletion during softening compared to earlier studies (e.g., Hyodo, Li, et al., 2013). Observed differences in hardening-softening characteristics could result from composition and grain size distribution of the sand or from GH formation procedures. Frequently in past studies, GH was formed prior to

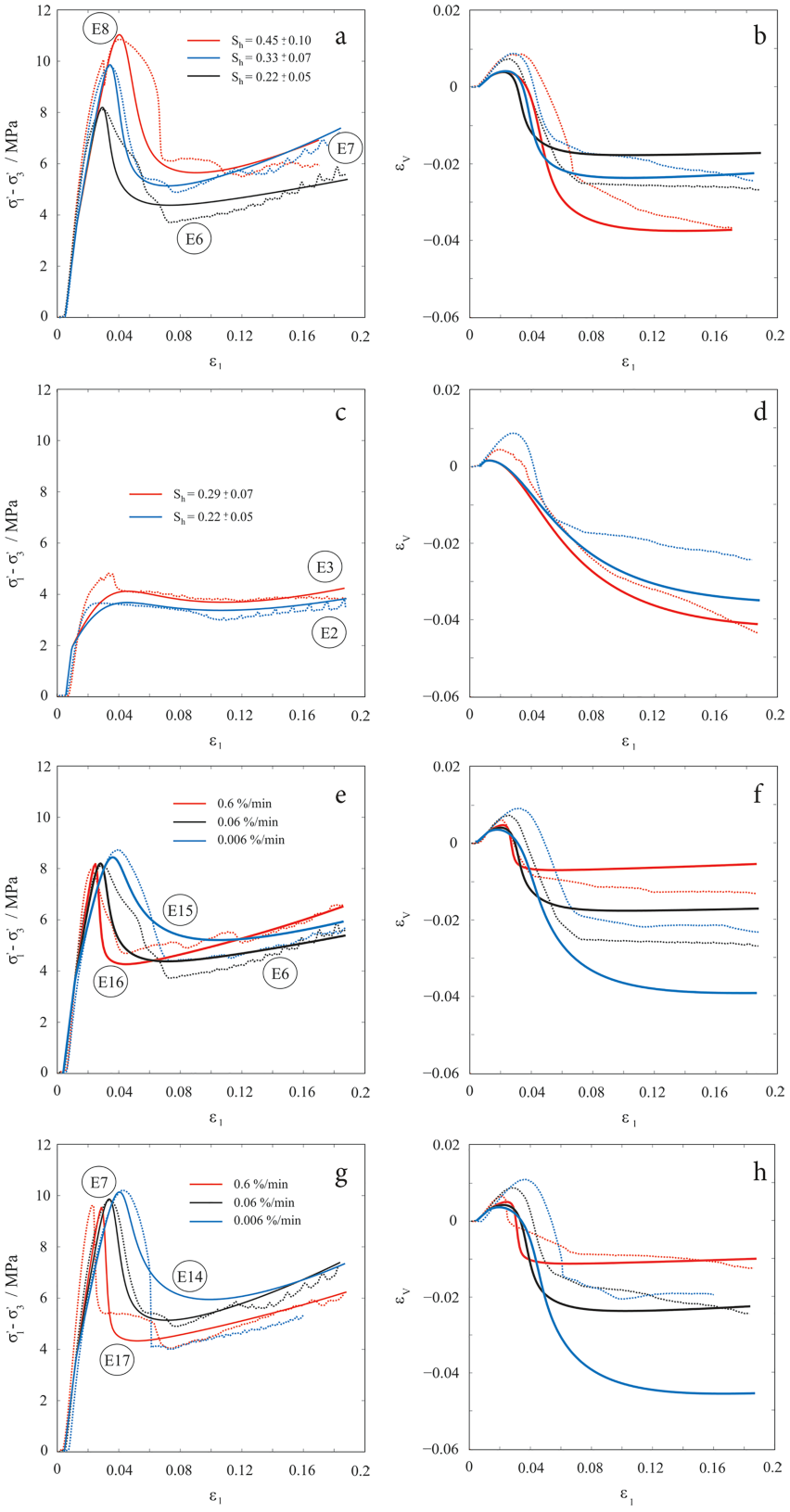

Figure 5. Simulation results for compression tests with different S_h and different strain rates. Gas-saturated samples: (a) strength characteristics and (b) volumetric strain; water-saturated samples: (c) strength characteristics and (d) volumetric strain. $S_h = 0.22$: (e) Strength characteristics and (f) volumetric strain; $S_h = 0.33$–0.36: (g) Strength characteristics and (h) volumetric strain. (Solid lines: Simulation results. Dotted lines: Experimental data)

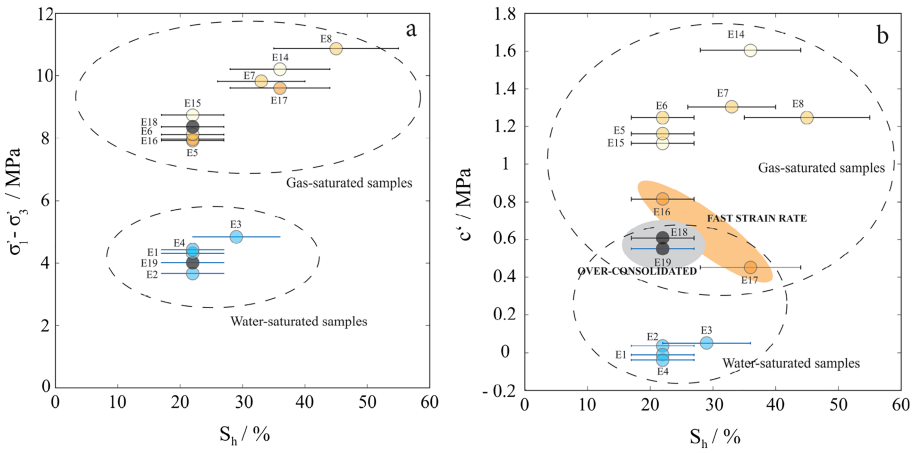

Figure 6. Peak strength and structuration effects. (a) The magnitude of peak strength (σ_1-σ_3) is dependent on GH saturation and pore fluid composition. (b) Transient increase of isotropic effective stress by 1 order of magnitude to 10 MPa (overconsolidated samples) degrades the structuration effect in gas-saturated GHBS (gray ellipse) and enhances the structuration effect in water-saturated sediments. Fast strain rates result in low structuration strength (orange ellipse). Grouping does not have a statistical meaning and is only included for illustrative purpose. Labels refer to test numbers in supporting information Tables S1–S3.

consolidation and formation was started from a frozen sample specimen (Hyodo, Li, et al., 2013; Miyazaki, Masui, et al., 2011; Priest et al., 2006). Consolidation after GH formation might, in contrast to consolidation before GH formation, result in different strength characteristics of GHBS, since consolidation could affect GH-sediment fabrics. However, evidence for this assumption is still lacking (Hyodo, Yoneda, et al., 2013). GH formation time intervals in this study (3–15 days) were substantially longer than in earlier studies (usually 24 h, Hyodo et al., 2014; Masui et al., 2005; Miyazaki, Masui, et al., 2011). In our studies, GH formation was clearly not completed after 24 h, which suggests that GH formation must have been faster in other studies. However, the results from this study indicate that the length of hold times after GH formation enables further strengthening of GH-sediment fabrics, potentially resulting from restructuration of GH through Ostwald ripening. Overall, this study confirms that GH alteration during aging changes the mechanical characteristics of GHBS and must be considered for the mechanical assessment of natural GHBS.

The hardening-softening behavior of the GHBS was clearly influenced by strain rates with substantial differences in loading-unloading behavior depending on the axial strain rate. The analysis of stress-strain behavior based on Rowe's stress-dilatancy theory suggests that GHs contribute a structuration effect in GHBS. This effect was substantial in water-limited systems with structuration strength (c') up to 2 MPa at the onset of dilation and 1.6 MPa at peak strength (Figure 6b and supporting information Table S3), which was high compared to results from other experimental studies with GHBS (e.g., Choi et al., 2018; Ghiassian & Grozic, 2013; Kajiyama, Wu, et al., 2017; Yoneda et al., 2016). However, in water-saturated specimen c' was substantially lower, reaching values of 0.4 MPa at the onset of dilation and 0.6 MPa at peak strength. In accordance to that, the test results clearly showed a delayed dilation, which is typical also for cemented sands (Lade & Trads, 2014; Leroueil & Vaughan, 1990; Wang & Leung, 2008). Interestingly, in our studies we observe a conspicuous secondary hardening response of GHBS, which was characterized by partial or even full recovery of apparent structuration strength.

The overall stress-strain behavior of GHBS in this study suggests that GH structures and GH-sediment fabrics dynamically rearrange in response to specific strain histories and loading events, and sediment shear strength is influenced by how fast plastic deformation occurs. This strain rate dependency of hardening-softening characteristics should be considered in constitutive modeling of GHBS.

4.2. Potential Mechanisms of Hardening-Softening Behavior

The hardening-softening behavior of GHBS depends on microstructural characteristics of the GH-sediment fabrics and is influenced by GH formation and sediment loading histories. Hardening-softening

characteristics and stress-strain behavior of GHBS in natural environments could be influenced by dynamic GH formation when sediment yielding results in the redistribution of pore fluids, since GH formation is rapid within GH stability boundaries given the presence of GH-forming molecules in contact with water (supporting information Figure S4 and Table S1). Residual water estimates from calculation of GH inventories indicate the presence of small amounts of water at the onset of the compression tests in this study (2.3 and supporting information S4). Thus, the observed hardening-softening characteristics and strength recovery were potentially affected by dynamic GH formation with residual water in response to fluid redistribution during plastic yielding, similar to what is expected for natural GHBS. Differences in compression test results with GHBS after different hold times (3–15 days, supporting information Figure S9) confirm that GH aging in the absence of net GH formation likewise influences the mechanical behavior and must be considered.

The structural and mechanical details of GHBS hardening-softening behavior are not fully understood, and it is unclear to what extent mechanical effects are to be attributed to changes in friction, dilatancy, or structuration parameters in constitutive modeling. This study suggests that the dynamic alteration and regeneration of GH-sediment fabrics strongly influence the hardening-softening behavior, leading to continuous rearrangement and restrengthening of GHBS during yielding events. Whereas at similar S_h the magnitude of peak strength was similar at strain rates between 0.006 and 0.6%/min, residual strength, softening characteristics, and apparent strength recovery were clearly different. At the highest shear rate the sample specimen showed very high stiffness and brittle failure characteristics, with rapid softening and mobilization of dilatancy after passing the point of peak strength. However, after only partial unloading the dilation response was suspended above residual strength values of reference samples. At slower strain rates the sample ductility was enhanced and correlated with slower and more extended mobilization of dilatancy.

In agreement with earlier studies (Miyazaki et al., 2017), we hypothesize that the alteration of GH-sediment structures during plastic deformation can partly be assigned to creep and viscous deformation of GH. In contrast to our results with gas-saturated samples, former studies with water-saturated samples indicate higher peak strength values at faster strain rates (Miyazaki et al., 2010), which suggests that strain-induced alteration of GH structures in water-saturated sediments is different from gas-saturated systems. This is in agreement with our observation of different hardening characteristics of GHBS after pore fluid exchange, which is proposed to result from dynamic alteration of GH-sediment fabrics during yielding. The differences in softening behavior with only partial unloading at fast strain rates indicate that the regeneration of GH-sediment fabrics depends on the rate of strength mobilization and unloading. We hypothesize that the brittle behavior and rapid softening at fast shear rates is influenced by transient GH dissociation through thermal stimulation or depressurization in a narrow dilation or shear zone (Figure 7). This argument is similar to Miyazaki et al. (2010), who suggest that load-induced heating at grain contacts causes GH dissociation. Transient dissociation and immediate reformation of GHs during brittle softening at fast shear rates could explain suppressed dilatancy and higher post-peak residual strength. Estimates for the local temperature increase from frictional heating in the shear zone suggest that 0.5–1.6 J/cm^2 could be dissipated as heat, which is in agreement with energy requirements to increase the temperature by 10 K in a layer of 1–2 mean particle diameters (supporting information Figure S10 and see also supporting information S10 for calculations). However, compared to gas-saturated systems it is less likely that heat dissipation from shear movements would be sufficient to trigger fast GH dissociation in water-saturated sediments, because the heat capacity of water would prevent T increase and destabilization of GH. Similar to thermal stimulation, GH dissociation in the shear zone could be caused by a local decrease in pore pressure during fast mobilization of dilatancy and increase in sediment volume. In this case, GH reformation would occur once pore pressure has recovered in response to local pressure gradients and sediment permeability. Clearly, thermal stimulation and depressurization in the shear zone are complementary mechanisms, and the overall stress-strain behavior could be a response to both mechanisms acting simultaneously.

Since softening intervals were followed by the apparent recovery of peak structuration strength, independent of cumulative axial strain at failure, we consider that also this large-strain behavior was influenced by the successive structural rearrangement of GH, once the dilatancy in the shear zone was mobilized. However, this secondary hardening response could be related to experimental artifacts during large-strain sample deformation, strain localization, and progression of failure. Since GHBS could be loaded to higher deviatoric stresses than reference samples and particle crushing is supposed to be inhibited in intact GHBS, particle

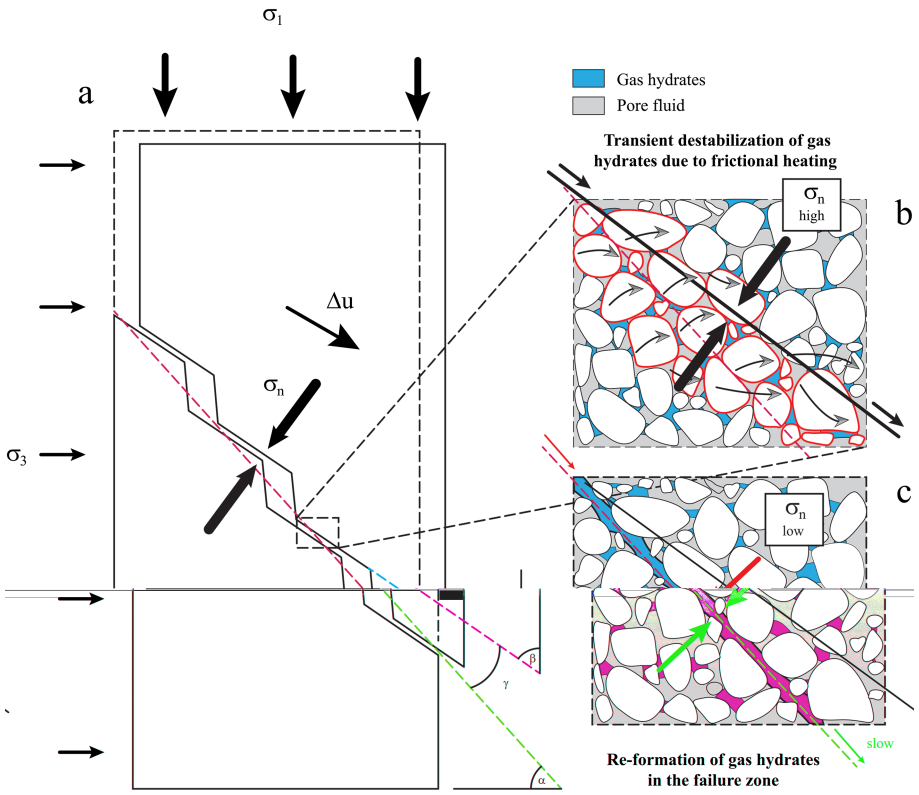

Figure 7. Model assumptions relevant for frictional heating during fast and brittle softening. (a) Saw-tooth model after Rowe (1962); figure modified after De Josselin De Jong (1976), (b) frictional heating and transient GH dissociation in a narrow shear zone after structuration strength depletion during softening and fast dilatancy mobilization, and (c) GH reformation and strength recovery in the shear zone.

crushing could occur rapidly and locally in the shear zone during unloading and failure. This would decrease the local void ratio and presumably change the mechanical properties. However, since secondary hardening was largely independent of peak stress ratios η, we suppose that particle crushing only played a minor role. Still, if it would be relevant it would need to be considered as a secondary effect of GH dynamics, and it would be treated similarly in the context of constitutive modeling. Further, we consider that our results at larger strains could be biased by the experimental setup to some extent. First, we use a combination of two sleeves for sample mounting in the triaxial cell. The inner sleeve is a FKM sleeve (thickness 1.5 mm) that is used to prepare and mount the sample without freezing. The outer sleeve is a latex sleeve (thickness 1 mm), which improves the sealing and avoids leakage of hydraulic fluid (glycol-water) into the sample pore space over long experimental periods. This combination of sleeves could increase the apparent strength of the sample during deformation. However, we tested if sleeve effects could explain the observed apparent secondary hardening using reference samples (test cylinders with predefined shear planes at 30°, 45°, or 60°) but could not find evidence for that (data no shown). Second, the axial strain is transferred through fixed platens that restrict the deformation of the sample. The use of fixed platens can influence strain localization and induce barreling or multiple shear banding (Alshibli et al., 2003; Gao & Zhao, 2013). In addition, individual experiments could be influenced by bedding errors and heterogeneity of GH formation. However, the similarity between individual tests and the onset of apparent secondary hardening after softening independent of the cumulative axial strain suggest that these effects would be minor.

4.3. The Concept of Nonconstant Residual Friction of GHBS

The hardening-softening behavior of GHBS appears to be controlled by dynamic changes of GH-sediment fabrics during plastic strain events. These strain and strain rate-dependent effects from alteration,

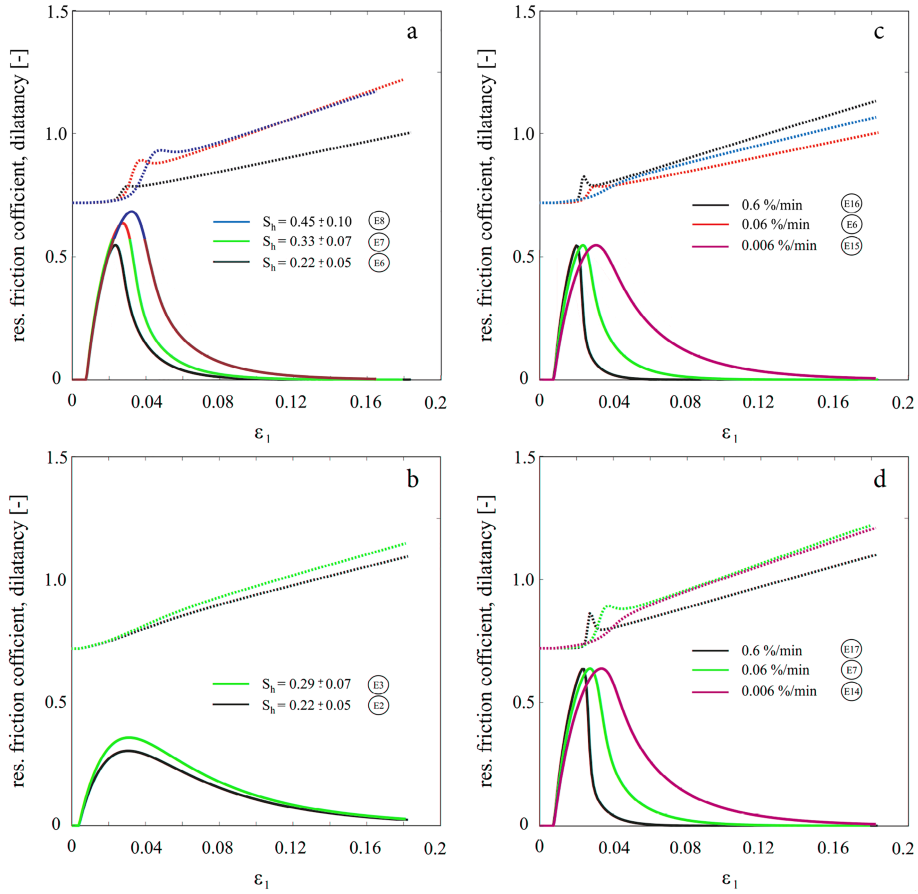

Figure 8. Residual friction (α_{res}, dotted lines) and dilation (β, thin lines) coefficients. (a) Gas-saturated samples, (b) water-saturated samples, (c) different strain rates, $S_h = 0.22$, and (d) different strain rates, $S_h = 0.33$–0.36.

rearrangement, and reformation of GH in the sediment matrix were conceptualized as nonconstant residual friction in elasto-plastic constitutive modeling by extending the approach of Andrade, et al. (2012), who considered rate-dependent residual friction for describing the fluid-like plasticity of granular media, for example, during shear banding.

The evolution functions for dilatancy and residual friction (equations (14) and (15)) postulate that the primary hardening occurs due to the dilatancy of the sample, while the softening and strength recovery occur due to an increase in residual frictional resistance under plastic loading depending on the plastic strain and strain rates (Figure 8). The cumulative volumetric strain was largely different in the individual experiments, and tests with GHBS usually showed lower overall cumulative strains and distinct shear banding compared to reference sand samples. Despite these differences in cumulative volumetric strains, peak dilatancy β_{max} was very similar, which suggests that the differences in stress-strain behavior at different S_h were not strongly related to changes in dilatancy.

Hardening-softening characteristics, strain localization, shear band evolution, and post-peak failure appear to be strongly dependent on strains and strain rates. Once dilatancy was fully mobilized inside the shear band and the cumulative volumetric strain remained to be largely constant, the residual friction α_{res} increased at a constant rate and resulted in apparent strength recovery in the shear band (Figure 8). For a given loading rate, there is a clear difference in the evolution of α_{res} between the gas-saturated and the water-saturated samples (see Figures 8a and 8b). In the gas-saturated samples, α_{res} increased abruptly for loading beyond the peak strength, whereas, for the water-saturated samples, the evolution of α_{res} is rather smooth. In general, the slower the rate at which dilatancy is mobilized, the smoother is the evolution of residual friction. This trend is also visible in Figures 8c and 8d, where at lower axial strain rates the dilatancy is mobilized

at a lower rate, and the evolution of the residual friction is smoother. The parameters $\Delta\alpha_{res}$ and $\dot{\lambda}^*$ control the evolution of α_{res} (refer to equation (15)). In Table 1, we observe that $\Delta\alpha_{res}$ shows a direct correlation with both S_h and the axial strain rate, while $\dot{\lambda}^*$ directly correlates only with the axial strain rate and appears to be independent of S_h. While this correlation appears to be straightforward, the combined effect on the evolution of α_{res} is in fact quite complex, and additional experimental data are required for further model calibration.

The microstructural aspects of GH alteration are currently unknown, and the micromechanical concepts are speculative and would require thorough micromechanical investigations, as well as mathematical homogenization and upscaling studies. However, we propose that the assumption of a nonconstant residual friction could act as a unifying concept, which also appears to be a reasonable basis for further model refinement as soon as data from geotechnical testing with high-resolution tomographical imaging become available in the future.

5. Conclusion

This study shows that strain rate-dependent effects influence the hardening-softening characteristics and stress-strain behavior of GHBS. We propose that this strain rate-dependency results from dynamic structural alterations of GH-sediment fabrics and provide evidence that brittleness and ductility characteristics during softening, shear band evolution, and strength recovery are influenced by the capacity of structural recovery of GH-sediment fabrics.

We hypothesize that the stress-strain response of GHBS on a micromechanical level is very complex and dependent on various processes and process interactions. Thus, it is very important to apply advanced geotechnical testing devices with tomographical imaging tools for time-resolved analysis of deformation and shear band development. However, we propose that on the level of constitutive modeling the dynamic alteration of GH-sediment fabrics can be conceptualized as a nonconstant residual friction term. In fact, we hypothesize that introducing the unifying concept of nonconstant residual friction might also advance the physical understanding of the apparent structuration strength of GHBS.

Our findings are highly relevant for the understanding of mechanical properties of natural GHBS, marine slope stability, and natural gas production scenarios. The recovery of strength of GHBS during plastic deformation and failure is supposed to act as an efficient self-stabilizing mechanism, which would be characterized by fast strength recovery in the event of fast deformation, and high residual strength in the presence of high S_h. Thus, the structural recovery of GH-sediment fabrics through slow rearrangement or fast dissociation-reformation events in the failure zone is expected to mitigate or counteract large-strain deformation of natural GHBS. This strain-induced self-stabilizing effect would be most pronounced in water-limited sediments, for example, in natural environments at marine gas seeps or in gas production scenarios.

Acknowledgments
Data are available in the PANGAEA open access data library (https://doi.pangaea.de/10.1594/PANGAEA.907074). We thank Mogens Schlund for his excellent support in the laboratory. We thank the Editor U. Faul and two anonymous reviewers for providing constructive and insightful comments and suggestions. This work was funded by the German Federal Ministry for Economic Affairs and Energy (BMWi) and Federal Ministry of Education and Research (BMBF) through the SUGAR project (grants 03SX250, 03SX320A, and 03G0856A), and the EU-FP7 project MIDAS (grant agreement 603418). We also acknowledge the support of the Cluster of Excellence *The Future Ocean* for funding the work of S. Gupta. *The Future Ocean* is funded within the framework of the Excellence Initiative by the Deutsche Forschungsgemeinschaft (DFG) on behalf of the German federal and state governments. Additional funding was received through the NSFC/RGC Joint Research Scheme (Project N_PolyU518/16).

References

Alshibli, K. A., Batiste, S. N., & Sture, S. (2003). Strain localization in sand: Plane strain versus triaxial compression. *Journal of Geotechnical and Geoenvironmental Engineering*, *129*(6), 483–494.

Andrade, J. E., Chen, Q., Le, P. H., Avila, C. F., & Matthew Evans, T. (2012). On the rheology of dilative granular media: Bridging solid- and fluid-like behavior. *Journal of the Mechanics and Physics of Solids*, *60*(6), 1122–1136.

Bastian, P., Heimann, F., & Marnach, S. (2010). Generic implementation of finite element methods in the Distributed and Unified Numerics Environment (DUNE). *Kybernetika*, *46*(2), 294–315.

Bolton, M. D. (1986). The strength and dilatancy of sands. *Geotechnique*, *36*(1), 65–78.

Boswell, R., Schoderbek, D., Collett, T. S., Ohtsuki, S., White, M., & Anderson, B. J. (2017). The Iġnik Sikumi field experiment, Alaska North Slope: Design, operations, and implications for CO_2-CH_4 exchange in gas hydrate reservoirs. *Energy and Fuels*, *31*(1), 140–153.

Brugada, J., Cheng, Y. P., Soga, K., & Santamarina, J. C. (2010). Discrete element modelling of geomechanical behaviour of methane hydrate soils with pore-filling hydrate distribution. *Granular Matter*, *12*(5), 517–525.

Bugge, T., Belderson, R. H., & Kenyon, N. H. (1988). The Storegga slide. *Philosophical Transactions - Royal Society, Series A*, *325*(1586), 358–ca.390.

Chaouachi, M., Falenty, A., Sell, K., Enzmann, F., Kersten, M., Haberthuer, D., & Kuhs, W. F. (2015). Microstructural evolution of gas hydrates in sedimentary matrices observed with synchrotron X-ray computed tomographic microscopy. *Geochemistry, Geophysics, Geosystems*, *16*, 1711–1722. https://doi.org/10.1002/2015GC005811

Choi, J. H., Dai, S., Cha, J. H., & Seol, Y. (2014). Laboratory formation of noncementing hydrates in sandy sediments. *Geochemistry, Geophysics, Geosystems*, *15*, 1648–1656. https://doi.org/10.1002/2014GC005287

Choi, J. H., Dai, S., Lin, J. S., & Seol, Y. (2018). Multistage triaxial tests on laboratory-formed methane hydrate-bearing sediments. *Journal of Geophysical Research: Solid Earth*, *123*, 3347–3357. https://doi.org/10.1029/2018JB015525

Clayton, C. R. I., Priest, J. A., & Best, A. I. (2005). The effects of disseminated methane hydrate on the dynamic stiffness and damping of a sand. *Geotechnique*, *55*(6), 423–434.

Collett, T. S. (2002). Energy resource potential of natural gas hydrates. *AAPG Bulletin*, *86*(11), 1971–1992.

Dai, S., Santamarina, J. C., Waite, W. F., & Kneafsey, T. J. (2012). Hydrate morphology: Physical properties of sands with patchy hydrate saturation. *Journal of Geophysical Research*, *117*, B11205. https://doi.org/10.1029/2012JB009667

De Josselin De Jong, G. (1976). Rowe's stress-dilatancy relation based on friction. *Geotechnique*, *26*(3), 527–534.

de Souza Neto, E. A., Peric, D., & Owen, D. R. J.(2008). *Computational Methods for Plasticity: Theory and Applications*. Chichester: Wiley & Sons Ltd.

Dedner, A., Flemisch, B., & Klöfkorn, V. (2010). Advances in DUNE, paper presented at Proceedings of the DUNE User Meeting, Springer Berlin Heidelberg, Stuttgart, Germany.

Deusner, C., Bigalke, N., Kossel, E., & Haeckel, M. (2012). Methane production from gas hydrate deposits through injection of supercritical CO_2. *Energies*, *5*(7), 2112–2140.

Deusner, C., Gupta, S., Kossel, E., Haeckel, M., Freise, M., Anbergen, H., & Wille, T. (2017). Advanced mechanical testing of gas hydrate-bearing sediments, paper presented at ICSMGE 2017-19th International Conference on Soil Mechanics and Geotechnical Engineering.

Deusner, C., Kossel, E., Bigalke, N., Haeckel, M., Gupta, S., Freise, M., et al. (2016). The role of high-pressure flow-through experiments for evaluating the mechanical behaviour of gas hydrate-bearing soils, paper presented at Energy Geotechnics—Proceedings of the 1 st International Conference on Energy Geotechnics, ICEGT 2016.

Durham, W. B., Kirby, S. H., Stern, L. A., & Zhang, W. (2003). The strength and rheology of methane clathrate hydrate. *Journal of Geophysical Research*, *108*(4), 2182. https://doi.org/10.1029/2002JB001872

Ebinuma, T., Kamata, Y., Minagawa, H., Ohmura, R., Nagao, J., & Narita, H. (2005). Mechanical properties of sandy sediment containing methane hydrate, paper presented at Proceedings of the Fifth International Conference on Gas Hydrates.

Elger, J., Berndt, C., Rüpke, L., Krastel, S., Gross, F., & Geissler, W. H. (2018). Submarine slope failures due to pipe structure formation. *Nature Communications*, *9*(1), 715. https://doi.org/10.1038/s41467-018-03176-1

Fujii, T., Suzuki, K., Takayama, T., Tamaki, M., Komatsu, Y., Konno, Y., et al. (2015). Geological setting and characterization of a methane hydrate reservoir distributed at the first offshore production test site on the Daini-Atsumi Knoll in the eastern Nankai Trough, Japan. *Marine and Petroleum Geology*, *66*, 310–322.

Gao, Z., & Zhao, J. (2013). Strain localization and fabric evolution in sand. *International Journal of Solids and Structures*, *50*(22-23), 3634–3648.

Ghiassian, H., & Grozic, J. L. H. (2013). Strength behavior of methane hydrate bearing sand in undrained triaxial testing. *Marine and Petroleum Geology*, *43*, 310–319.

Gupta, S., Deusner, C., Haeckel, M., Helmig, R., & Wohlmuth, B. (2017). Testing a thermo-chemo-hydro-geomechanical model for gas hydrate-bearing sediments using triaxial compression laboratory experiments. *Geochemistry, Geophysics, Geosystems*, *18*, 3419–3437. https://doi.org/10.1002/2017GC006901

Gupta, S., Helmig, R., & Wohlmuth, B. (2015). Non-isothermal, multi-phase, multi-component flows through deformable methane hydrate reservoirs. *Computational Geosciences*, *19*(5), 1063–1088.

Houlsby, G.T. (1991). How the dilatancy of soils affects their behaviour, invited theme lecture, Proceedings of the Tenth European Conference on Soil Mechanics and Foundation Engineering, Florence, May 27-30, 4, 1189-1202

Huang, J., & Griffiths, D. V. (2009). Return mapping algorithms and stress predictors for failure analysis in geomechanics. *Journal of Engineering Mechanics*, *135*(4), 276–284.

Hyodo, M., Li, Y., Yoneda, J., Nakata, Y., Yoshimoto, N., & Nishimura, A. (2014). Effects of dissociation on the shear strength and deformation behavior of methane hydrate-bearing sediments. *Marine and Petroleum Geology*, *51*, 52–62.

Hyodo, M., Li, Y., Yoneda, J., Nakata, Y., Yoshimoto, N., Nishimura, A., & Song, Y. (2013). Mechanical behavior of gas-saturated methane hydrate-bearing sediments. *Journal of Geophysical Research: Solid Earth*, *118*, 5185–5194. https://doi.org/10.1002/2013JB010233

Hyodo, M., Wu, Y., Nakashima, K., Kajiyama, S., & Nakata, Y. (2017). Influence of fines content on the mechanical behavior of methane hydrate-bearing sediments. *Journal of Geophysical Research: Solid Earth*, *122*, 7511–7524. https://doi.org/10.1002/2017JB014154

Hyodo, M., Yoneda, J., Yoshimoto, N., & Nakata, Y. (2013). Mechanical and dissociation properties of methane hydrate-bearing sand in deep seabed. *Soils and Foundations*, *53*(2), 299–314.

Inada, N., & Yamamoto, K. (2015). Data report: Hybrid Pressure Coring System tool review and summary of recovery result from gas-hydrate related coring in the Nankai project. *Marine and Petroleum Geology*, *66*, 323–345.

Ito, T., Komatsu, Y., Fujii, T., Suzuki, K., Egawa, K., Nakatsuka, Y., et al. (2015). Lithological features of hydrate-bearing sediments and their relationship with gas hydrate saturation in the eastern Nankai trough, Japan. *Marine and Petroleum Geology*, *66*, 368–378. https://doi.org/10.1016/j.marpetgeo.2015.02.022

Jia, J., Liang, Y., Tsuji, T., Murata, S., & Matsuoka, T. (2016). Microscopic origin of strain hardening in methane hydrate. *Scientific Reports*, *6*.

Jia, J., Liang, Y., Tsuji, T., Murata, S., & Matsuoka, T. (2017). Elasticity and stability of clathrate hydrate: Role of guest molecule motions. *Scientific Reports*, *7*(1).

Jiang, M., Sun, C., Crosta, G. B., & Zhang, W. (2015). A study of submarine steep slope failures triggered by thermal dissociation of methane hydrates using a coupled CFD-DEM approach. *Engineering Geology*, *190*, 1–16.

Jiang, M., Zhu, F., & Utili, S. (2015). Investigation into the effect of backpressure on the mechanical behavior of methane-hydrate-bearing sediments via DEM analyses. *Computers and Geotechnics*, *69*, 551–563.

Jirasek, M., & Bazant, Z. P. (2002). *Inelastic analysis of structures*. Chichester: John Wiley & Sons, Ltd.

Jung, J. W., Jang, J., Santamarina, J. C., Tsouris, C., Phelps, T. J., & Rawn, C. J. (2012). Gas production from hydrate-bearing sediments: The role of fine particles. *Energy and Fuels*, *26*(1), 480–487.

Jung, J. W., & Santamarina, J. C. (2011). Hydrate adhesive and tensile strengths. *Geochemistry, Geophysics, Geosystems*, *12*, Q08003. https://doi.org/10.1029/2010GC003495

Kajiyama, S., Hyodo, M., Nakata, Y., Yoshimoto, N., Wu, Y., & Kato, A. (2017). Shear behaviour of methane hydrate bearing sand with various particle characteristics and fines. *Soils and Foundations*, *57*(2), 176–193.

Kajiyama, S., Wu, Y., Hyodo, M., Nakata, Y., Nakashima, K., & Yoshimoto, N. (2017). Experimental investigation on the mechanical properties of methane hydrate-bearing sand formed with rounded particles. *Journal of Natural Gas Science and Engineering*, *45*, 96–107.

Kimoto, S., Oka, F., & Fushita, T. (2010). A chemo-thermo-mechanically coupled analysis of ground deformation induced by gas hydrate dissociation. *International Journal of Mechanical Sciences*, *52*(2), 365–376.

Klar, A., Soga, K., & Ng, M. Y. A. (2010). Coupled deformation-flow analysis for methane hydrate extraction. *Geotechnique*, *60*(10), 765–776.
Klar, A., Uchida, S., Soga, K., & Yamamoto, K. (2013). Explicitly coupled thermal flow mechanical formulation for gas-hydrate sediments. *SPE Journal*, *18*(2), 196–206.
Konno, Y., Fujii, T., Sato, A., Akamine, K., Naiki, M., Masuda, Y., et al. (2017). Key findings of the world's first offshore methane hydrate production test off the coast of Japan: Toward future commercial production. *Energy and Fuels*, *31*(3), 2607–2616.
Kuhn, H. W., & Tucker, A. W. (1951). Nonlinear programming, paper presented at Proceedings of the Second Berkeley Symposium on Mathematical Statistics and Probability, University of California Press, Berkeley, Calif., *1951*.
Kvalstad, T. J., Andresen, L., Forsberg, C. F., Berg, K., Bryn, P., & Wangen, M. (2005). The Storegga slide: Evaluation of triggering sources and slide mechanics. *Marine and Petroleum Geology*, *22*(1-2 SPEC. ISS), 245–256.
Lade, P. V., & Trads, N. (2014). The role of cementation in the behaviour of cemented soils. *Geotechnical Research*, *1*(4), 111–132.
Lee, J. Y., Francisca, F. M., Santamarina, J. C., & Ruppel, C. (2010). Parametric study of the physical properties of hydrate-bearing sand, silt, and clay sediments: 2. Small-strain mechanical properties. *Journal of Geophysical Research*, *115*, B11105. https://doi.org/10.1029/2009JB006670
Lee, J. Y., Santamarina, J. C., & Ruppel, C. (2010). Parametric study of the physical properties of hydrate-bearing sand, silt, and clay sediments: 1. Electromagnetic properties. *Journal of Geophysical Research*, *115*, B11104. https://doi.org/10.1029/2009JB006669
Lei, L., Seol, Y., Choi, J. H., & Kneafsey, T. J. (2019). Pore habit of methane hydrate and its evolution in sediment matrix—Laboratory visualization with phase-contrast micro-CT. *Marine and Petroleum Geology*, *104*, 451–467.
Lei, L., Seol, Y., & Jarvis, K. (2018). Pore-scale visualization of methane hydrate-bearing sediments with micro-CT. *Geophysical Research Letters*, *45*, 5417–5426. https://doi.org/10.1029/2018GL078507
Leroueil, S., & Vaughan, P. R. (1990). The general and congruent effects of structure in natural soils and weak rocks. *Geotechnique*, *40*(3), 467–488.
Lin, J. S., Seol, Y., & Choi, J. H. (2015). An SMP critical state model for methane hydrate-bearing sands. *International Journal for Numerical and Analytical Methods in Geomechanics*, *39*(9), 969–987.
Masui, A., Haneda, H., Ogata, Y., & Aoki, K. (2005). Effects of methane hydrate formation on shear strength of synthetic methane hydrate sediments, paper presented at Proceedings of the International Offshore and Polar Engineering Conference.
McConnell, D. R., Zhang, Z., & Boswell, R. (2012). Review of progress in evaluating gas hydrate drilling hazards. *Marine and Petroleum Geology*, *34*(1), 209–223.
Miyazaki, K., Aoki, K., Tenma, N, Sakamoto, Y., & Yamaguchi, T. (2011). Application of nonlinear elastic constitutive model to analysis of artificial methane-hydrate-bearing sediment sample, paper presented at Proceedings of the ISOPE Ocean Mining Symposium.
Miyazaki, K., Masui, A., Aoki, K., Sakamoto, Y., Yamaguchi, T., & Okubo, S. (2010). Strain-rate dependence of triaxial compressive strength of artificial methane-hydrate-bearing sediment. *International Journal of Offshore and Polar Engineering*, *20*(4), 256–264.
Miyazaki, K., Masui, A., Sakamoto, Y., Aoki, K., Tenma, N., & Yamaguchi, T. (2011). Triaxial compressive properties of artificial methane-hydrate-bearing sediment. *Journal of Geophysical Research*, *116*, B06102. https://doi.org/10.1029/2010JB008049
Miyazaki, K., Tenma, N., Aoki, K., Sakamoto, Y., & Yamaguchi, T. (2011). Effects of confining pressure on mechanical properties of artificial methane-hydrate-bearing sediment in triaxial compression test. *International Journal of Offshore and Polar Engineering*, *21*(2), 148–154.
Miyazaki, K., Tenma, N., & Yamaguchi, T. (2017). Relationship between creep property and loading-rate dependence of strength of artificial methane-hydrate-bearing toyoura sand under triaxial compression. *Energies*, *10*(10).
Mountjoy, J. J., Pecher, I., Henrys, S., Crutchley, G., Barnes, P. M., & Plaza-Faverola, A. (2014). Shallow methane hydrate system controls ongoing, downslope sediment transport in a low-velocity active submarine landslide complex, Hikurangi Margin, New Zealand. *Geochemistry, Geophysics, Geosystems*, *15*, 4137–4156. https://doi.org/10.1002/2014GC005379
Ning, F., Yu, Y., Kjelstrup, S., Vlugt, T. J. H., & Glavatskiy, K. (2012). Mechanical properties of clathrate hydrates: Status and perspectives. *Energy and Environmental Science*, *5*(5), 6779–6795.
Omidvar, M., Iskander, M., & Bless, S. (2012). Stress-strain behavior of sand at high strain rates. *International Journal of Impact Engineering*, *49*, 192–213.
Pinkert, S. (2017). The lack of true cohesion in hydrate-bearing sands. *Granular Matter*, *19*(3).
Porcino, D. D., & Marcianò, V. (2017). Bonding degradation and stress–dilatancy response of weakly cemented sands. *Geomechanics and Geoengineering*, *12*(4), 221–233.
Priest, J. A., Best, A. I., & Clayton, C. R. I. (2006). Attenuation of seismic waves in methane gas hydrate-bearing sand. *Geophysical Journal International*, *164*(1), 149–159.
Priest, J. A., Rees, E. V. L., & Clayton, C. R. I. (2009). Influence of gas hydrate morphology on the seismic velocities of sands. *Journal of Geophysical Research*, *114*, B11205. https://doi.org/10.1029/2009JB006284
Rowe, P. W. (1962). The stress-dilatancy relation for static equilibrium of an assembly of particles in contact. *Proceedings of the Royal Society of London. Series A: Mathematical and Physical Sciences*, *269*(1339), 500.
Rutqvist, J., Moridis, G. J., Grover, T., & Collett, T. (2009). Geomechanical response of permafrost-associated hydrate deposits to depressurization-induced gas production. *Journal of Petroleum Science and Engineering*, *67*(1-2), 1–12.
Rutqvist, J., Moridis, G. J., Grover, T., Silpngarmlert, S., Collett, T. S., & Holdich, S. A. (2012). Coupled multiphase fluid flow and wellbore stability analysis associated with gas production from oceanic hydrate-bearing sediments. *Journal of Petroleum Science and Engineering*, *92-93*, 65–81.
Sánchez, M., Gai, X., & Santamarina, J. C. (2017). A constitutive mechanical model for gas hydrate bearing sediments incorporating inelastic mechanisms. *Computers and Geotechnics*, *84*, 28–46.
Santamarina, J., & Ruppel, C. (2010). 26. The impact of hydrate saturation on the mechanical, electrical, and thermal properties of hydrate-bearing sand, silts, and clay. In M. Riedel, E. C. Willoughby & S. Chopra(Eds.), *Geophysical Characterization of Gas Hydrates* (pp. 373-384), *Society of Exploration Geophysicists*. Tulsa: Society of Exploration Geophysicists
Santamarina, J. C., Dai, S., Terzariol, M., Jang, J., Waite, W. F., Winters, W. J., et al. (2015). Hydro-bio-geomechanical properties of hydrate-bearing sediments from Nankai trough. *Marine and Petroleum Geology*, *66*, 434–450. https://doi.org/10.1016/j.marpetgeo.2015.02.033
Schanz, T., & Vermeer, P. A. (1996). Angles of friction and dilatancy of sand. *Geotechnique*, *46*(1), 145–151.
Schoderbek, D., Martin, K. L., Howard, J., Silpngarmlert, S., & Hester, K. (2012). North slope hydrate fieldtrial: CO_2/CH_4 exchange, paper presented at Society of Petroleum Engineers - Arctic Technology Conference 2012.
Shen, Z., & Jiang, M. (2016). DEM simulation of bonded granular material. Part II: Extension to grain-coating type methane hydrate bearing sand. *Computers and Geotechnics*, *75*, 225–243.
Shen, Z., Jiang, M., & Thornton, C. (2016). DEM simulation of bonded granular material. Part I: Contact model and application to cemented sand. *Computers and Geotechnics*, *75*, 192–209.

Simo, J. C., & Hughes, T. J. R. (2006). *Computational inelasticity*. New York: Springer.
Song, Y., Zhu, Y., Liu, W., Li, Y., Lu, Y., & Shen, Z. (2016). The effects of methane hydrate dissociation at different temperatures on the stability of porous sediments. *Journal of Petroleum Science and Engineering*, *147*, 77–86.
Song, Y., Zhu, Y., Liu, W., Zhao, J., Li, Y., Chen, Y., et al. (2014). Experimental research on the mechanical properties of methane hydrate-bearing sediments during hydrate dissociation. *Marine and Petroleum Geology*, *51*, 70–78.
Stern, L. A., Kirby, S. H., & Durham, W. B. (1996). Peculiarities of methane clathrate hydrate formation and solid-state deformation, including possible superheating of water ice. *Science*, *273*(5283), 1843–1848.
Sultan, N., & Garziglia, S. (2014). Mechanical behaviour of gas-charged fine sediments: Model formulation and calibration. *Geotechnique*, *64*(11), 851–864.
Sun, X., Guo, X., Shao, L., & Tang, H. (2015). A thermodynamics-based critical state constitutive model for methane hydrate bearing sediment. *Journal of Natural Gas Science and Engineering*, *27*, 1024–1034.
Suzuki, K., Schultheiss, P., Nakatsuka, Y., Ito, T., Egawa, K., Holland, M., & Yamamoto, K. (2015). Physical properties and sedimentological features of hydrate-bearing samples recovered from the first gas hydrate production test site on Daini-Atsumi Knoll around eastern Nankai trough. *Marine and Petroleum Geology*, *66*, 346–357.
Teixeira Parente, M., Mattis, S., Gupta, S., Deusner, C., & Wohlmuth, B. (2018). Efficient parameter estimation for a methane hydrate model with active subspaces. *Computational Geosciences*, *23*(2), 355–372.
Uchida, S., Klar, A., & Yamamoto, K. (2016). Sand production modeling of the 2013 nankai offshore gas production test, paper presented at Energy Geotechnics—Proceedings of the 1 st International Conference on Energy Geotechnics, ICEGT 2016.
Uchida, S., Soga, K., & Yamamoto, K. (2012). Critical state soil constitutive model for methane hydrate soil. *Journal of Geophysical Research*, *117*, B03209. https://doi.org/10.1029/2011JB008661
Waite, W. F., Santamarina, J. C., Cortes, D. D., Dugan, B., Espinoza, D. N., Germaine, J., et al. (2009). Physical properties of hydrate-bearing sediments. *Reviews of Geophysics*, *47*, RG4003. https://doi.org/10.1029/2008RG000279
Waite, W. F., Winters, W. J., & Mason, D. H. (2004). Methane hydrate formation in partially water-saturated Ottawa sand. *American Mineralogist*, *89*(8-9), 1202–1207.
Wallmann, K., Pinero, E., Burwicz, E., Haeckel, M., Hensen, C., Dale, A., & Ruepke, L. (2012). The global inventory of methane hydrate in marine sediments: A theoretical approach. *Energies*, *5*(7), 2449–2498.
Wang, Y. H., & Leung, S. C. (2008). Characterization of cemented sand by experimental and numerical investigations. *Journal of Geotechnical and Geoenvironmental Engineering*, *134*(7), 992–1004.
Winters, W. J., Waite, W. F., Mason, D. H., Gilbert, L. Y., & Pecher, I. A. (2007). Methane gas hydrate effect on sediment acoustic and strength properties. *Journal of Petroleum Science and Engineering*, *56*(1-3), 127–135.
Wojciechowski, M. (2018). A note on the differences between Drucker-Prager and Mohr-Coulomb shear strength criteria. *Studia Geotechnica et Mechanica*, *40*(3), 163–169.
Yamamoto, K., Terao, Y., Fujii, T., Ikawa, T., Seki, M., Matsuzawa, M., & Kanno, T. (2014). Operational overview of the first offshore production test of methane hydrates in the eastern Nankai trough, paper presented at Proceedings of the Annual Offshore Technology Conference.
Yoneda, J., Jin, Y., Katagiri, J., & Tenma, N. (2016). Strengthening mechanism of cemented hydrate-bearing sand at microscales. *Geophysical Research Letters*, *43*, 7442–7450. https://doi.org/10.1002/2016GL069951
Yoneda, J., Masui, A., Konno, Y., Jin, Y., Egawa, K., Kida, M., et al. (2015a). Mechanical properties of hydrate-bearing turbidite reservoir in the first gas production test site of the eastern Nankai trough. *Marine and Petroleum Geology*, *66*, 471–486.
Yoneda, J., Masui, A., Konno, Y., Jin, Y., Egawa, K., Kida, M., et al. (2015b). Mechanical behavior of hydrate-bearing pressure-core sediments visualized under triaxial compression. *Marine and Petroleum Geology*, *66*, 451–459.
Yu, F., Song, Y., Liu, W., Li, Y., & Lam, W. (2011). Analyses of stress strain behavior and constitutive model of artificial methane hydrate. *Journal of Petroleum Science and Engineering*, *77*(2), 183–188.
Yu, H. S., Tan, S. M., & Schnaid, F. (2007). A critical state framework for modelling bonded geomaterials. *Geomechanics and Geoengineering*, *2*(1), 61–74.
Yun, T. S., Santamarina, C. J., & Ruppel, C. (2007). Mechanical properties of sand, silt, and clay containing tetrahydrofuran hydrate. *Journal of Geophysical Research*, *112*, B04106. https://doi.org/10.1029/2006JB004484
Zander, T., Choi, J. C., Vanneste, M., Berndt, C., Dannowski, A., Carlton, B., & Bialas, J. (2018). Potential impacts of gas hydrate exploitation on slope stability in the Danube deep-sea fan, Black Sea. *Marine and Petroleum Geology*, *92*, 1056–1068.
Zienkiewicz, O. C., & Taylor, R. L. (2014). *The finite element method for solid and structural mechanics*. Oxford: Butterworth-Heinemann.